

Molecular Dynamics Simulation of Titanium Dioxide Nanoparticle Sintering

Vishal N. Koparde* and Peter T. Cummings

Department of Chemical Engineering, Vanderbilt University, VU Station B 351604, Nashville, Tennessee 37235

Received: August 18, 2005; In Final Form: October 27, 2005

Nanoparticles have been an area of active research in recent years due to their properties, which can be greatly different from the bulk. In this work, we study the sintering of TiO₂ nanoparticles using molecular dynamics simulations. Such sintering occurs in flame reactors where nanotitania is prepared via the chloride process. Decrease in free energy due to reduction in surface area is the main driving force for sintering of particles. Simulations, at various starting temperatures and orientations, indicate that the process of sintering is strongly affected by temperature and initial orientation. Extremely high diffusion of ions in the neck region of sintering nanoparticles supports the idea that solid-state diffusion is significant in metal-oxide nanoparticle sintering. It is found that the dipole–dipole interaction between sintering nanoparticles plays a very important role at temperatures away from the melting point. The duration of the simulation is not enough to observe the complete sintering process, but important initial stages are well studied.

Introduction

Interest in the physics of nanoscale condensed matter, which is at size scales larger than individual atoms or molecules but much smaller than bulk solids, has developed rapidly in the past three decades.^{1–5} The fact that controlling the size of solids in the range 1–100 nm could considerably alter their physical and chemical properties is the impetus behind this growing curiosity.^{3,6,7} The applications of nanoscale condensed matter are quickly growing in the fields of medicine,^{8,9} electrochemistry,¹⁰ electronics,¹¹ and aerospace.¹² Titanium dioxide is a widely occurring metal-oxide semiconductor. Due to its opacity, it has been used as a white pigment in paints^{13–17} and papers; however, nowadays, nanosized titania is widely used as a raw material in electronic and structural ceramics.¹⁸ It is also used in dye-sensitized solar cells and in high-temperature separation and photocatalytic applications.^{1,15,19–27} Recently, nanosized titania has been used as a catalyst in many different reactions under ultraviolet light, such as alcohol dehydration,²⁸ degradation of paint pigments,²⁹ oxidation of aromatic compounds,³⁰ nitrogen oxide reduction,³¹ and removal of toxic contaminants from wastewater.^{25,26}

It has been reported in the literature that seven different polymorphs of titania exist. Six of them have a distinct structure.^{23–27,32} Those found in nature are anatase, rutile, and brookite.^{17,22,33–38} The structure of anatase and rutile is tetragonal, while brookite is orthorhombic.^{13,17,34,35,38} In the bulk form, rutile is the most stable polymorph of titania while anatase and brookite are considered to be metastable,^{13,17,18,21,33–35,38–40} transforming exothermally and irreversibly to rutile upon heating.^{17,21,41} The stability criterion is dependent on the particle size, and it has been found experimentally that in the nanocrystalline form anatase is the most stable polymorph.³⁸ The electronic and photocatalytic properties of titania are rapidly enhanced as the size diminishes.

Nanosized titania is manufactured by either a dry or a wet process.^{13,24,42,43} The dry process, also called the chloride process, involves vapor phase oxidation reaction of TiCl₄, which leads to the production of amorphous nanotitania, which is then annealed to get the desired phase. The temperatures range from

973 to 1873 K in this process.^{1,14,15,40,44,45} About 3 million tons of TiO₂ are produced annually via this process.⁴⁶ The reaction involved in this process can be represented as^{15,16,40,44–46}



Understanding the details of this process is necessary for optimizing the reaction conditions and obtaining a high-quality product.⁴⁶ During the thermal annealing following the chloride process, the titania nanoparticles collide with each other and sintering occurs, forming larger particles or agglomerates. If the sintering time is less than the collision time, then larger particles are produced; otherwise, agglomerates, consisting of smaller particles fused together, are formed.⁴⁷ There are many theories explaining the process of sintering, but they may not be applicable to the material under consideration due to the small size of these particles. Thus, the questions regarding the nature of growth kinetics and morphology are of great concern.^{48,49} It has been shown that colliding submicron particles cannot be treated as continuum elastic bodies and the fact that they are composed of individual atoms is important.⁵⁰ Therefore, here, we study the process of sintering of titanium dioxide nanoparticles from an atomic point of view using molecular dynamics simulation.

There are believed to be six different mechanisms⁵¹ contributing toward the sintering of larger particles, namely,

- (a) surface diffusion
- (b) lattice diffusion from surface
- (c) vapor transport
- (d) grain boundary diffusion
- (e) lattice diffusion from grain boundary
- (f) lattice diffusion through dislocations.

However, in smaller particles, the sintering mechanism is radically different due to the presence of high surface curvature and atomic forces becoming more significant. For Cu and Au nanoparticles, it is reported that surface and grain boundary diffusion are the most significant transport processes in nanoparticle sintering.⁵¹

The driving force for the sintering of two TiO₂ nanoparticles is the decrease in the free energy due to a reduction in the

surface area.⁵² Solid-state diffusion within the particle, which is due to the stress gradients generated by nonsphericity, is believed to be the controlling mechanism.⁵³ The resultant larger particle or agglomerate will have a lower potential energy and, due to conservation of energy in an isolated system, a higher temperature.⁴⁷ The temperature rise can also be explained by the formation of new chemical bonds between the particles after collision.^{47,54} Since TiO₂ nanoparticles coalesce by virtue of solid-state diffusion, which is extremely sensitive to temperature,⁵² one can expect that temperature will play a critical role in the process of nanoparticle sintering. Earlier studies on silica nanoparticle sintering showed almost instantaneous coalescence at higher temperatures⁵⁵ and fractal-like agglomerate formation at lower temperatures.⁴⁷ It was also found that the heat release due to particle coalescence may reduce the coalescence time by as much as a few orders of magnitude in the case of silicon nanoparticles.

There have been many models attempting to explain the dynamics of the coalescence of particles. Koch and Friedlander^{55,56} assumed that the rate of coalescence was directly related to the excess surface area of colliding particles. This simple linear decay law for the agglomerate surface area,⁵³ when combined with the aerosol general dynamics equation,¹⁴ has produced several successful models for particle size prediction. These models break down when the particle size goes down to a few nanometers. It was suggested that the high internal pressure of smaller particles could be responsible for the inapplicability of the models to smaller particles. For example, the pressure inside a 10 nm TiO₂ particle is reported to be around 2000 atm^{1,57} and it increases with decreasing size. Such high internal pressures affect the diffusion coefficients, which in turn affect the rates of particle sintering.^{6,57} Thus, atomistic studies of nanoparticles can shed light on the fundamental mechanisms of nanoparticle sintering, thereby providing valuable insights and guidance to experimental work.^{51,58} To date, very few simulation studies have actually probed the sintering of metal-oxide nanoparticles. Zhu and Averback^{58–60} carried out molecular dynamics simulations of sintering Cu particles, while Raut et al.⁶¹ reported studies of sintering aluminum particles. Similar studies of sintering nickel particles have been carried out by Heinisch.⁶²

In the work presented here, we are investigating the initial stages of TiO₂ sintering and the effect of phase, size, and temperature on the sintering process. In our simulations, we have only considered the anatase and rutile phases. The nanoparticle sizes considered are 3 and 4 nm. The systems under consideration contain two nanoparticles of the same phase. We then investigate the effect of orientation on sintering process by rotating one of the particles in the system while keeping the other unchanged. The relative mobilities of ions in the neck and core regions of the sintering nanoparticles are also reported.

Simulation Details

Force Field Selection. A survey of the literature shows that several force fields for TiO₂ have been published.^{33,63–71} A detailed in-depth assessment of the different available force fields has been carried out by Smith and co-workers.⁷² Their report concludes that the force field developed by Matsui and Akaogi³³ is the most suitable of the available force fields for use in classical molecular dynamics simulations of bulk titania. Swamy et al.³⁷ compared a variable-charge force field⁷⁰ for TiO₂ to the force field by Matsui–Akaogi and concluded that the Matsui–Akaogi force field performed better than the more complex variable-charge force field. The structures of the TiO₂

TABLE 1: Interaction Parameters for the Matsui–Akaogi Force Field

ion	q	A	B	C
Ti	+2.196	1.1823	0.077	22.5
O	−1.098	1.6339	0.117	54.0

polymorphs and their bulk relative stabilities predicted by the Matsui–Akaogi force field are within experimental limits when compared with the limited available experimental data.^{16,72} This force field was further verified using quantum mechanical methods by Bandura and Kubicki,⁷³ where they tested its suitability for surface studies. Hence, we infer that the Matsui–Akaogi force field is capable of representing both the bulk and the surface. This is crucial when dealing with finite size particles, as surface effects can no longer be overlooked. Consequently, we make use of the simple Matsui–Akaogi force field in our simulations. This rigid-ion model, in which the ions have partial fixed charges, can be rewritten in a site–site interaction form:

$$U(r_{ij}) = A_{ij} \exp\left(-\frac{r_{ij}}{\rho_{ij}}\right) - \frac{C_{ij}}{r_{ij}^6} + \frac{q_i q_j}{r_{ij}} \quad (2)$$

where $U(r_{ij})$ is the interaction energy between sites i and j and the parameters A_{ij} , ρ_{ij} , and C_{ij} are listed in Table 1. The charges, q 's, for titanium and oxygen are +2.196 and −1.098, respectively, in atomic units.

Simulation Method. To generate the nanoparticles, a sphere of the desired diameter is cut out of a larger lattice, which is constructed using the lattice parameters⁷⁴ for anatase and rutile. Excess titanium ions or oxygen ions are removed from the surface to obtain charge balance and ensure neutrality. Initially, molecular dynamics simulation in the canonical ensemble (NVT) is performed to obtain a nanoparticle at the desired temperature. Then, to generate the initial configuration for the sintering simulation of same phase nanoparticles, the sphere is replicated and translated along the x -axis, so that the distance between the surfaces of the replicas is 1 nm. DLPOLY, version 2.13,^{75,76} which uses Verlet's leapfrog algorithm for integration of Newton's equations of motion is used to carry out all the molecular dynamics simulations. Sintering simulations are carried out in the microcanonical ensemble (NVE) using a 0.5 fs time step, and no periodic boundary conditions are applied to ensure simulation of isolated nanoparticles. This is the best way to mimic the low-pressure conditions prevailing in the flame reactors of the chloride process. The cutoff is chosen such that all the ions in the system are included in force and energy calculations. Simulations were carried out for a total time of about 0.5 to 1 ns. This time is extremely small to study the entire process of TiO₂ nanoparticle sintering but is long enough to study the important initial stages of sintering. Furthermore, the potential energy reaches a plateau by this time (see Figure 1), indicating that the system is entering a quasi-steady state. Kobata et al.⁴⁰ suggests that the characteristic sintering time for 3 nm TiO₂ sintering at 1473 K is about 12 μ s, which is too long for a molecular dynamics simulation. In this work, various simulations with different starting temperatures, namely, 573, 973, and 1473 K, are carried out for 1 ns each to investigate the dependence of temperature; as in the flame synthesis process, there are different regions in the flame, representing different temperature zones, and the simulations are repeated for 3 and 4 nm particles because in the synthesis process particles of different sizes sinter and the effect of size is bound to be significant to the overall sintering process.

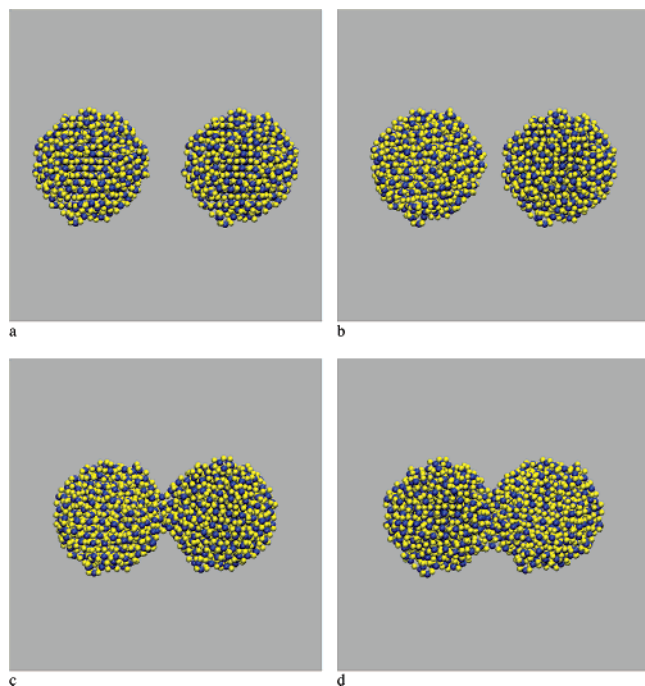


Figure 1. Snapshots of a typical nanoparticle sintering simulation.

Results and Discussion

Figure 1 shows snapshots of a typical sintering simulation. The simulation involves two 3 nm anatase nanoparticles with a starting temperature of 573 K. The simulation begins as shown in Figure 1a where the identical nanoparticles are separated by 1 nm, or in other words, the center-to-center distance between the 3 nm anatase nanoparticles is about 4 nm. We observe, as in Figure 1b, that the nanoparticles are mutually attracted toward each other. It should be noted that no external force is applied on any of the nanoparticles throughout the simulation. There is visual evidence of surface distortion, or increase in surface roughness, as the particles come in close proximity. The collision takes place in about 20–25 ps without any rebounding or fracturing. This is depicted in Figure 1c. A neck formation follows the collision, which quickly grows to a diameter of about 1.6 nm. A gradual broadening of the neck is observed in the period that follows to reach the final agglomerated state indicated in Figure 1d with a neck diameter of about 1.75 nm. The simulation is continued for a total time of about 0.5 ns, and complete fusion of the two anatase nanoparticles is not observed over the course of simulation, although we expect the formation of a larger spherical nanoparticle if the simulation is allowed to run for a very long time. Simulated X-ray diffraction patterns suggested that there is no phase transformation during the entire simulation.

Figure 2 shows the temperature and configurational energy of the system versus the time of simulation. The drop in the configurational energy occurs when the two nanoparticles touch each other for the first time and is caused by the new low-potential-energy pairs created when ions from each nanoparticle come in close proximity of each other. We observe that there is a rapid increase in temperature immediately after the nanoparticles come in contact with each other. As the nanoparticles form a neck, their cumulative surface area decreases, thereby decreasing their overall potential energy. Since the total energy of an isolated adiabatic system must be conserved, the kinetic energy goes up, in turn increasing the temperature of the system. The temperature rise is about 45 K for 3 nm particle sintering of rutile and anatase. For 4 nm particles, the temper-

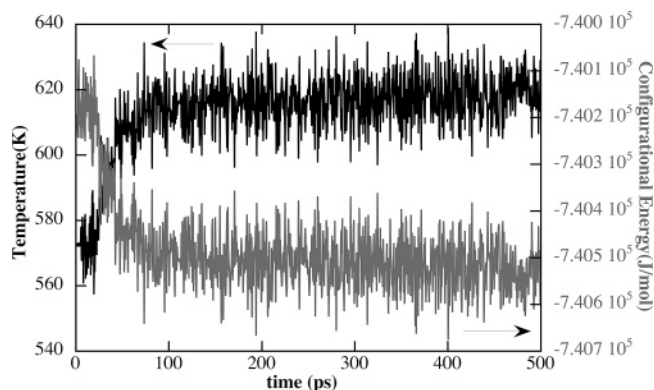


Figure 2. Time evolution of the temperature and configuration energy of the system.

ature rise is observed to be of the order of 30 K. Thus, the temperature rise upon neck formation seems to be decreasing with particle size. This is consistent with the temperature being given by the average kinetic energy per particle; hence, for larger particles, a given decrease in total potential energy (compensated by an equal increase in total kinetic energy) translates to a smaller increase in temperature. The temperature rise is however found to be independent of the starting temperature of the simulation. This is expected, since, as in all of the simulations with identical particle sizes, the decrease in surface area is similar; thereby, the amount of potential energy to be converted to kinetic energy upon agglomeration is almost the same. These figures also indicate that sintering of titania nanoparticles takes place in two steps. The first step is very rapid and involves the formation of the neck region, which leads to the sudden drop in the overall configurational energy of the system, and the second step includes all of the rearrangements that follow. The second step is very slow and cannot be studied over the course of our molecular dynamics simulations.

Shrinkage, Neck Diameter, and Number of Ions in the Neck Region. In earlier studies,⁶¹ shrinkage was defined as $\Delta L/L_0$, where L_0 is the distance between the centers of mass of the sintering nanoparticles and ΔL is the change in this distance with time. We modify this definition to

$$\text{shrinkage} = \frac{\left(\frac{d_1 + d_2}{2}\right) - d_{\text{COM}}}{\left(\frac{d_1 + d_2}{2}\right)} \quad (3)$$

where d_1 and d_2 are the diameters of the sintering nanoparticles while d_{COM} is the distance between their centers of mass at that instance. Thus, the shrinkage is negative when the nanoparticles are not touching each other, zero when they just touch each other for the first time, and positive when they start intermingling. Figures 3 and 4 show the shrinkage versus time plots of 3 and 4 nm particles, respectively, with various starting temperatures indicated in parentheses in the figures. There is limited dependence on starting temperature for the rutile particles. The shrinkage seems to be increasing with starting temperature for the 3 nm anatase particles. This is proposed to be due to higher interpenetration at higher temperatures due to greater solid diffusion.

Neck diameter increases with temperature for 3 nm anatase nanoparticles, ranging from 17 Å for a starting temperature of 573 K to about 22 Å for a starting temperature of 1473 K, while the neck diameter is almost independent of temperature in the case of 3 nm rutile nanoparticles, as interpreted from Figure 5.

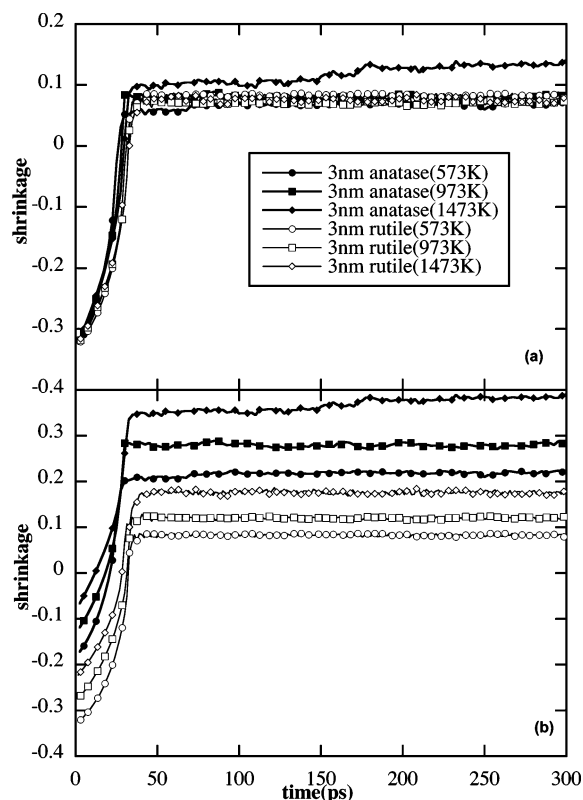


Figure 3. (a) Shrinkage vs time at various temperatures for 3 nm TiO_2 nanoparticles (starting temperatures indicated in parentheses). (b) The shrinkage curves are separated by 0.05 units for detailed viewing.

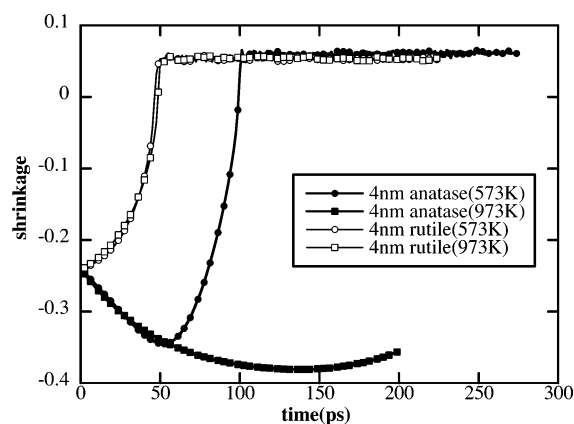


Figure 4. Shrinkage vs time at various temperatures for 4 nm TiO_2 nanoparticles (starting temperatures indicated in parentheses).

The number of ions in the neck regions seems to increase with temperature for 3 nm anatase particles, while there is no obvious dependence on temperature in the case of rutile particles, as shown in Figure 6. Simulated X-ray diffraction patterns were determined for the agglomerates at the end of the simulations. These patterns indicated that no phase change had occurred in any of the simulations. The neck region is also examined separately of phase change. These examinations suggest that the neck region between two anatase nanoparticles becomes amorphous while the neck region between two rutile nanoparticles remains rutile.

Dependence on Particle Orientation. It is believed that crystallographic orientation also plays a vital role in the sintering of crystalline nanoparticles. To study this effect, the duplicated particle in the simulation system was rotated about the z -axis through various angles, namely, 20, 45, 90, and 180°, before the start of the simulation. This ensured different crystallographic

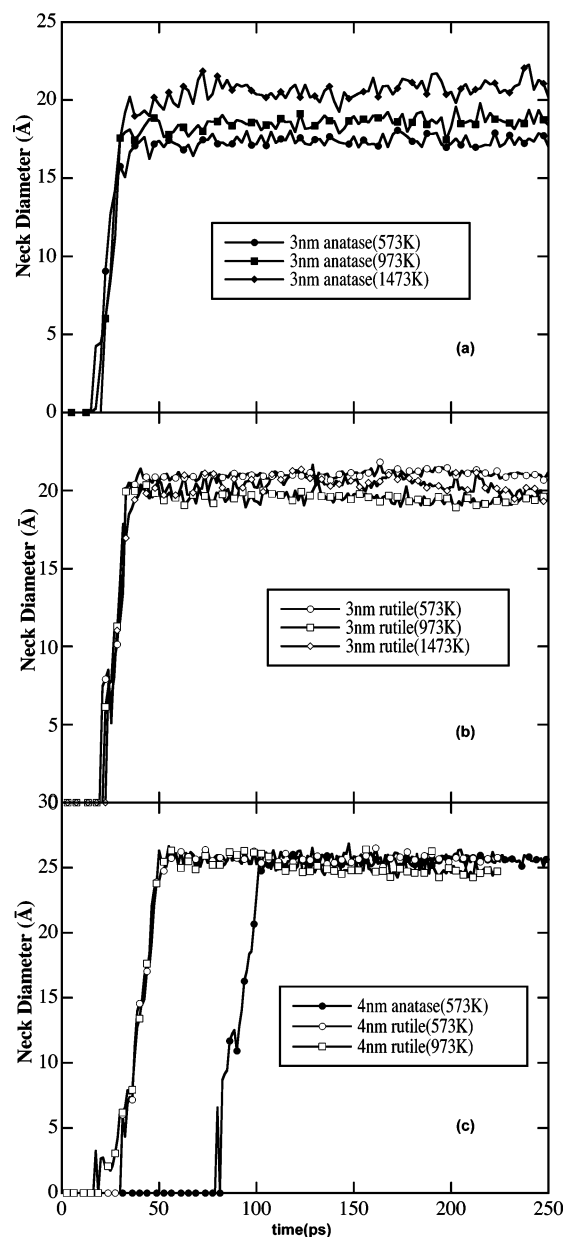


Figure 5. Neck diameters of sintering 3 nm anatase (a), rutile (b), and 4 nm (c) nanoparticles with different initial temperatures (initial temperatures indicated in parentheses).

orientations along the x -axis, which is the axis the particles approach each other, initially. Simulations were carried out for the 3 nm anatase particles for 0.5 ns as before. Neck formation occurred almost at the same time in all of the cases except the 180° rotation case. In this case, the particles moved away from each other and never collided over the period of the simulation. This suggests that orientation of the nanoparticles is extremely important in the process of sintering. This is further supported by Figure 7, which shows the shrinkages at various orientations. The orientation of 90° produced maximum interpenetration, suggesting that this initial configuration may be most favorable. Similar densification observed experimentally using X-ray diffraction of larger titania particles by Kumar et al.⁷⁷ is related to the anatase–rutile transformation, but we did not find any phase transformation over the course of our simulation based on the simulated X-ray diffraction patterns. It was found that the neck sizes were approximately identical for all orientations except 90°. Thus, except for the 90° case, the results seemed to be compatible with the idea that the surfaces of the particles

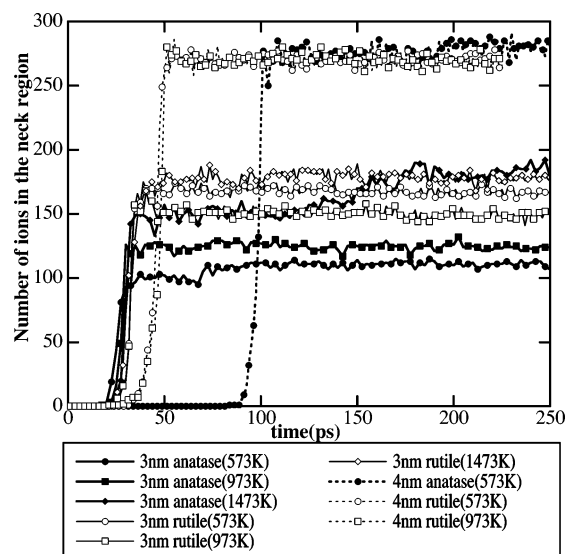


Figure 6. Number of ions in the neck region vs time for sintering anatase and rutile nanoparticles with different starting temperatures (initial temperatures indicated in parentheses).

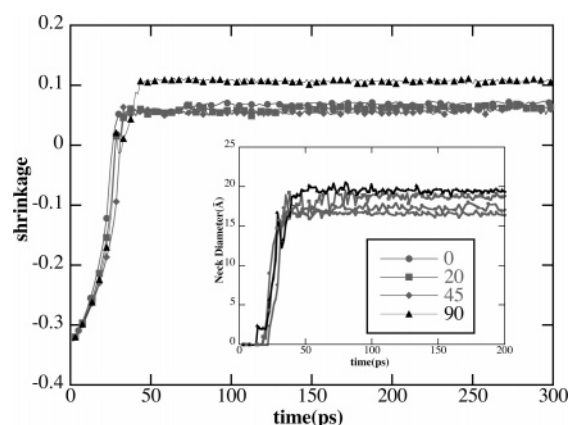


Figure 7. Effect of orientation angle on shrinkage and neck diameter.

are nanoscopically rough and so the rotation of particles does not affect their interaction with each other.

To interpret the dependence of orientation more clearly, the dipole–dipole interaction between the two interacting nanoparticles is determined. The dipole moment of each nanoparticle is given by

$$\bar{\mu} = \sum_i q_i \bar{r}_i \quad (4)$$

where $\bar{\mu}$ is the dipole moment of the particle, q_i is the charge on ion i , and \bar{r}_i is the position vector of ion i . The interaction energy between two dipoles is given by⁷⁸

$$W_{d-d} = \frac{\bar{\mu}_1 \cdot \bar{\mu}_2 - 3(\hat{n} \cdot \bar{\mu}_1)(\hat{n} \cdot \bar{\mu}_2)}{|\bar{r}_1 - \bar{r}_2|^3} \quad (5)$$

where $\bar{\mu}_1$ and $\bar{\mu}_2$ are the dipole moments of the particles, \bar{r}_1 and \bar{r}_2 are the position vectors of the centers of mass of the particles, and \hat{n} is the unit vector along $\bar{r}_1 - \bar{r}_2$. In general, the dipole–dipole interaction will be the dominant contribution to the long-range interaction between the particles. Figure 8 shows that as the angle of rotation was increased the dipole–dipole interaction became more repulsive and for 180° it was repulsive enough to prevent the particles from touching each other throughout the simulation. Also, the slightly repulsive configuration at 90°

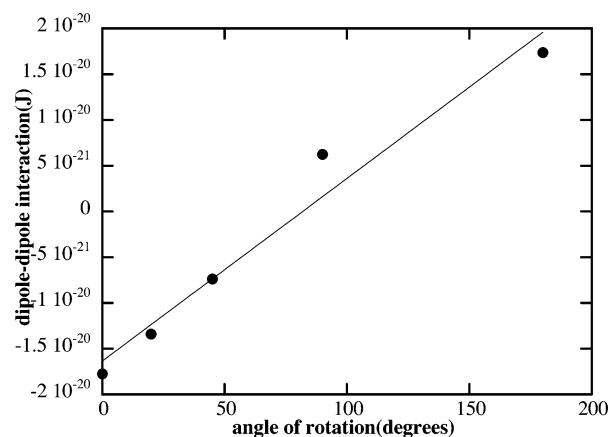


Figure 8. Variation of the dipole–dipole interaction of the nanoparticles at various initial orientations.

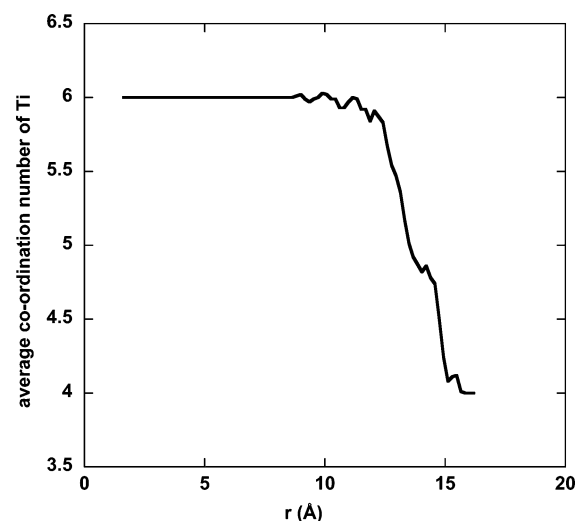


Figure 9. Radial variation of the titanium coordination number in a 3 nm anatase particle.

could explain why rotation and reorientation of particles was observed prior to neck formation. Temporal evolution of dipole–dipole interactions showed that these interactions gradually continued to become more attractive with time until shrinkage became zero. It may be possible to model TiO₂ nanoparticles as nanoscopic spheres with fluctuating dipole moments, interacting via eq 5, before they collide. Thus, the interparticle dipole–dipole interaction is very critical in the sintering dynamics of nanoparticles. This may not be the case for nanoparticles larger than 5 nm, as observed by Ogata et al.,⁷⁹ who suggest from their 6 nm particle simulations that surface charge effects dictate the course of nanoparticle sintering. Here, it should be noted that Ogata et al. used a variable-charge potential for their simulations in contrast to the rigid-ion-partial-charge potential used in this work.

Relative Mobilities in the Neck and Core Regions. To gain further insight into the sintering mechanism, the relative atomic mobilities in the neck and core region are calculated. All nanoparticles in the simulations have a crystalline core and an amorphous surface. In anatase and rutile lattices, the coordination number of the titanium ion is 6. Figure 9 shows the variation of the coordination number of the titanium ion in a 3 nm anatase particle along the radius of the nanoparticle. The external region where the coordination number starts going below 6 can be considered as amorphous. Simulation results show that the thickness of this amorphous region, which is about the order of 3–3.5 Å, is independent of size and temperature. Thus, ions

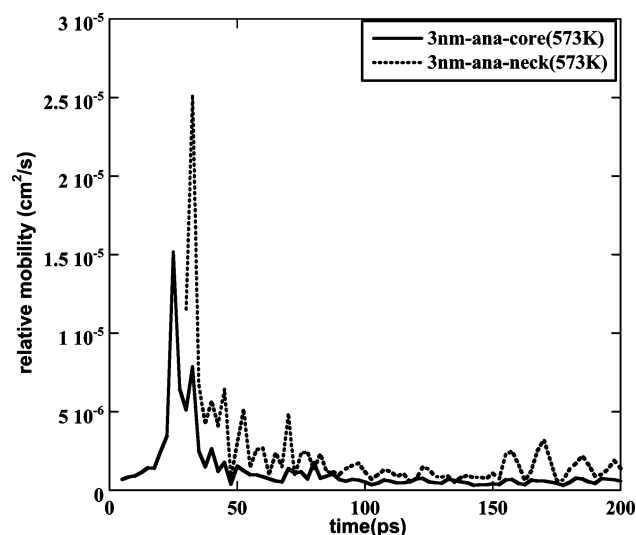


Figure 10. Relative mobilities of Ti ions in the core and neck regions for a 3 nm anatase sintering simulation with an initial temperature of 573 K.

within a distance less than 70% of the radius of the particle from the center of mass of the particle are considered to be in the core region of the particle. All of the ions within 3 Å of the orthogonal plane bisecting the line connecting centers of mass of the two sintering nanoparticles are considered to be in the neck region. Following Zhu and Averback,⁵⁸ the relative displacement of the i th ion from time t to t' is calculated as

$$\Delta r_i(t, t') = \sqrt{\left((r_i(t) - r_i(t')) - \frac{1}{m_{\text{Ti}}n'_{\text{Ti}} + m_{\text{O}}n'_{\text{O}}} \left(\sum_{j=1}^{n'_{\text{Ti}}} m_{\text{Ti}}(r_j(t) - r_j(t')) + \sum_{k=1}^{n'_{\text{O}}} m_{\text{O}}(r_k(t) - r_k(t')) \right) \right)^2} \quad (6)$$

The relative displacements of the titanium ions, in the neck and core regions, in a typical sintering simulation are shown in Figure 10. The initial peak suggests fast motion of the ions upon first contact between sintering particles. It should also be noted that the neck region relative ionic mobility remains more than the core region relative ionic mobility throughout the simulation. Figures 11 and 12 compare the core and neck region mobilities for sintering anatase and rutile 3 nm particles, respectively. Similar figures comparing the core and neck region mobilities for sintering anatase and rutile 4 nm particles have been provided in Supporting Information Figures 1S and 2S, respectively. The relative mobility in the neck region does not show any significant dependence on size or phase but seems to be increasing with the initial temperature of the particles.

Concluding Remarks

We have tried to shed light upon a number of interesting details pertaining to the sintering characteristics of TiO₂ nanoparticles. The study shows that the sintering of anatase and rutile nanoparticles is very rapid and occurs in a few picoseconds. The initial stage of the sintering process involves neck formation, upon first contact, followed by gradual particle interpenetration and broadening of the neck region. The temperature rise upon sintering is found to be independent of the initial temperature of the sintering particles but dependent on the particle size. Higher initial temperatures promote greater

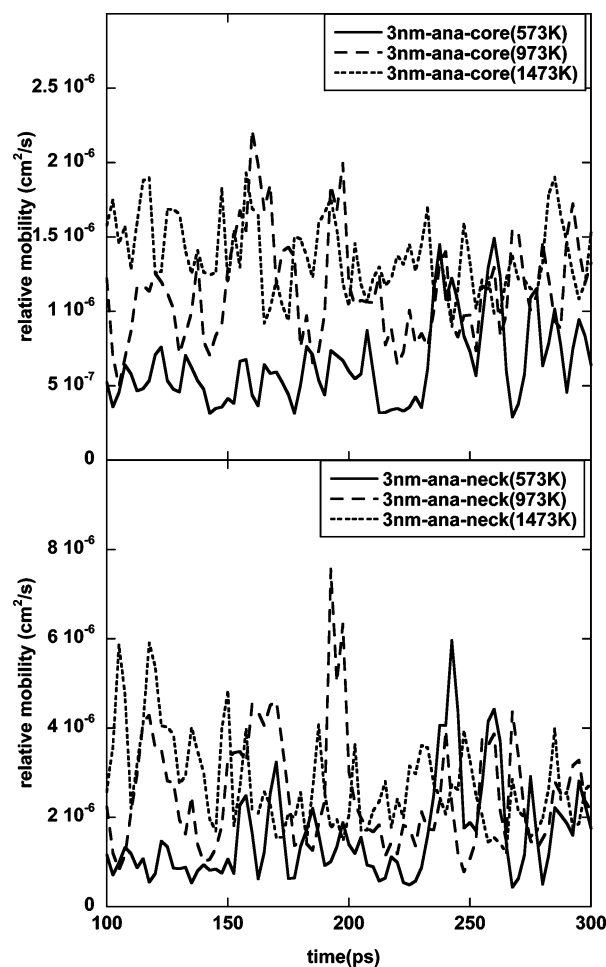


Figure 11. Comparison of the relative mobilities of Ti ions in the core and neck regions for various anatase nanoparticle simulations.

intermingling of anatase particles leading to larger neck sizes and higher shrinkage. No such dependence is observed for rutile particles. The relative orientation of sintering nanoparticles seems to highly influence the shrinkage and the neck sizes, suggesting that there may be a higher extent of surface diffusion for certain orientations rather than others. In the simulations considered here, the dipole–dipole interactions between nanoparticles are found to play a very important role in nanoparticle sintering. It may be possible to model titania nanoparticles as spheres with fluctuating dipole moments that undergo collision before the onset of sintering. We plan to run simulations with larger titania nanoparticles in the future to examine if the contribution from dipole–dipole interaction toward nanoparticle sintering diminishes with nanoparticle size.

Two particle systems are useful for studying the isolated sintering process, but systems with a larger number of particles with periodic boundary conditions could be employed in the future to study many-particle sintering. Future efforts could be directed toward correlating the various observations and developing scaling laws for sintering at the nanoscales that can be applied to phenomenological models of particle sintering.

Acknowledgment. We would like to acknowledge National Science Foundation (EAR- 0308539) for the funding for this work and the National Energy Research Scientific Computing Center for providing computer time to run the simulations.

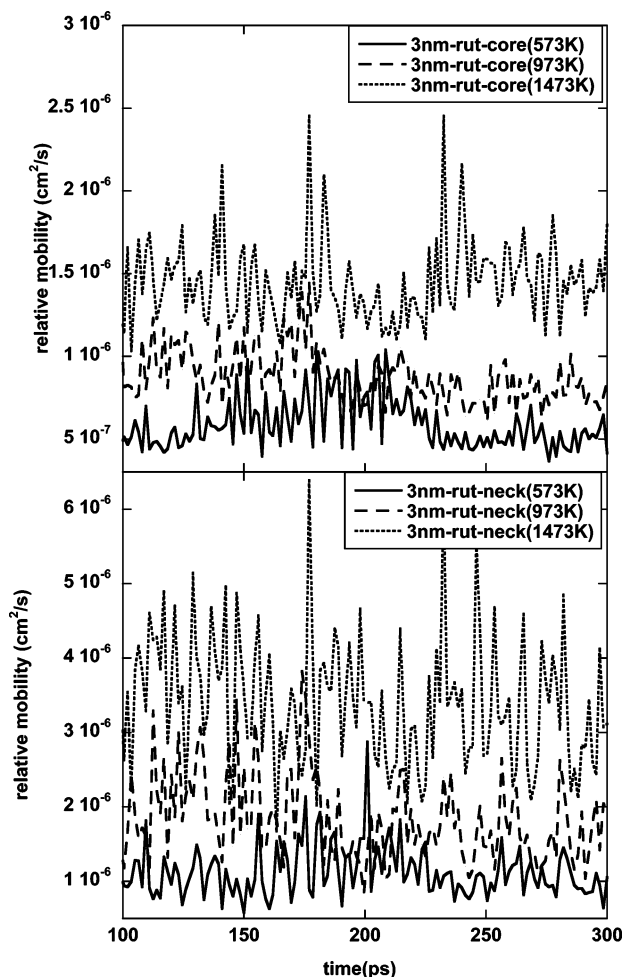


Figure 12. Comparison of the relative mobilities of Ti ions in the core and neck regions for various rutile nanoparticle simulations.

Supporting Information Available: Figures which compare the core and neck region mobilities for sintering 4 nm anatase and rutile, respectively, and a movie showing the sintering of two 3 nm anatase nanoparticles with a starting temperature of 1473 K. In this movie, the titanium ions, which are in the neck region at the end of the simulation, are colored green, the oxygen ions, which are in the neck region at the end of the simulation, are colored red, and all other ions are colored white. Thus, this movie also emphasizes the solid-state diffusion occurring in these simulations. This material is available free of charge via the Internet at <http://pubs.acs.org>.

References and Notes

- (1) Ding, X. Z.; Liu, X. H. *J. Alloys Compd.* **1997**, *248*, 143.
- (2) Siegel, R. W. *Phys. Today* **1993**, *46*, 64.
- (3) Siegel, R. W.; Sanders, P. G.; Witney, A. B.; et al. *Mater. Sci. Eng., A* **1995**, *204*, 7.
- (4) Dewdney, A. K. *Sci. Am.* **1988**, *258*, 100.
- (5) Franks, A. *J. Phys. E: Sci. Instrum.* **1987**, *20*, 1442.
- (6) Schweigert, I. V.; Lehtinen, K. E. J.; Carrier, M. J.; et al. *Phys. Rev. B* **2002**, *65*.
- (7) Oakley, B. A.; Hanna, D. M. *IEEE Trans. Nanobiosci.* **2004**, *3*, 74.
- (8) Sahoo, S. K.; Labhasetwar, V. *Drug Discovery Today* **2003**, *8*, 1112.
- (9) Silva, G. A. *Surg. Neurol.* **2004**, *61*, 216.
- (10) Gooding, J. J. *Electrochim. Acta* **2005**, *50*, 3049.
- (11) Tsukagoshi, K.; Yoneya, N.; Uryu, S.; et al. *Physica B* **2002**, *323*, 107.
- (12) Laurvick, C. A.; Singaraju, B. *IEEE Aerospace Electron. Syst. Mag.* **2003**, *18*, 18.
- (13) Kolen'ko, Y. V.; Burukhin, A. A.; Churagulov, B. R.; et al. *Mater. Lett.* **2003**, *57*, 1124.
- (14) Akhtar, M. K.; Yun, X. O.; Pratsinis, S. E. *AIChE J.* **1991**, *37*, 1561.
- (15) Collins, D. R.; Smith, D. J.; Harrison, N. M.; et al. *J. Mater. Chem.* **1997**, *7*, 2543.
- (16) Collins, D. R.; Smith, W.; Harrison, N. M.; et al. *J. Mater. Chem.* **1996**, *6*, 1385.
- (17) Cheng, H.; Ma, J.; Zhao, Z.; et al. *Chem. Mater.* **1995**, *7*, 663.
- (18) Zhang, H.; Banfield, J. F. *J. Mater. Chem.* **1998**, *8*, 2073.
- (19) Yang, J.; Mei, S.; Ferreira, J. M. F. *J. Mater. Res.* **2002**, *17*, 2197.
- (20) Yang, J.; Mei, S.; Ferreira, J. M. F. *J. Am. Ceram. Soc.* **2001**, *84*, 1696.
- (21) Yang, J.; Mei, S.; Ferreira, J. M. F. *J. Am. Ceram. Soc.* **2000**, *83*, 1361.
- (22) Wu, M. M.; Long, J. B.; Huang, A. H.; et al. *Langmuir* **1999**, *15*, 8822.
- (23) Yang, J.; Mei, S.; Ferreira, J. M. F. *Mater. Sci. Eng., C* **2001**, *15*, 183.
- (24) Yin, S.; Li, R. X.; He, Q. L.; et al. *Mater. Chem. Phys.* **2002**, *75*, 76.
- (25) Ohtani, B.; Okugawa, Y.; Nishimoto, S.; et al. *J. Phys. Chem.* **1987**, *91*, 3550.
- (26) Martin, S. T.; Lee, A. T.; Hoffmann, M. R. *Environ. Sci. Technol.* **1995**, *29*, 2567.
- (27) Augugliaro, V.; Loddo, V.; Palmisano, L.; et al. *J. Catal.* **1995**, *153*, 32.
- (28) Fox, M. A.; Dulay, M. T. *Chem. Rev.* **1993**, *93*, 341.
- (29) Hotsenpiller, P. A. M.; Bolt, J. D.; Farneth, W. E.; et al. *J. Phys. Chem. B* **1998**, *102*, 3216.
- (30) Fujihira, M.; Satoh, Y.; Osa, T. *Nature* **1981**, *293*, 206.
- (31) Gruy, F.; Pijolat, M. *J. Am. Ceram. Soc.* **1992**, *75*, 657.
- (32) Banfield, J. F.; Veblen, D. R.; Smith, D. J. *Am. Mineral.* **1991**, *76*, 343.
- (33) Matsui, M.; Akaogi, M. *Mol. Simul.* **1991**, *6*, 239.
- (34) Hu, Y.; Tsai, H. L.; Huang, C. L. *J. Eur. Ceram. Soc.* **2003**, *23*, 691.
- (35) Ding, X. Z.; Liu, X. H. *J. Mater. Res.* **1998**, *13*, 2556.
- (36) Freeman, C. M.; Newsam, J. M.; Levine, S. W.; et al. *J. Mater. Chem.* **1993**, *3*, 531.
- (37) Swamy, V.; Gale, J. D.; Dubrovinsky, L. S. *J. Phys. Chem. Solids* **2001**, *62*, 887.
- (38) Hu, Y.; Tsai, H. L.; Huang, C. L. *Mater. Sci. Eng., A* **2003**, *344*, 209.
- (39) Ovenstone, J. *J. Mater. Sci.* **2001**, *36*, 1325.
- (40) Kobata, A.; Kusakabe, K.; Morooka, S. *AIChE J.* **1991**, *37*, 347.
- (41) Shannon, R. D.; Paks, J. A. *J. Am. Ceram. Soc.* **1965**, *48*, 391.
- (42) Pratsinis, S. E. *Prog. Energy Combust. Sci.* **1998**, *24*, 197.
- (43) Stark, W. J.; Pratsinis, S. E. *Powder Technol.* **2002**, *126*, 103.
- (44) Jang, H. D. *AIChE J.* **1997**, *43*, 2704.
- (45) Jang, H. D.; Jeong, J. *Aerosol Sci. Technol.* **1995**, *23*, 553.
- (46) Pratsinis, S. E.; Spicer, P. T. *Chem. Eng. Sci.* **1998**, *53*, 1861.
- (47) Lehtinen, K. E. J.; Zachariah, M. R. *J. Aerosol Sci.* **2002**, *33*, 357.
- (48) Zachariah, M. R.; Carrier, M. J. *J. Aerosol Sci.* **1999**, *30*, 1139.
- (49) Zachariah, M. R.; Carrier, M. J.; BlaistenBarojas, E. *J. Phys. Chem.* **1996**, *100*, 14856.
- (50) Preining, O. *J. Aerosol Sci.* **1998**, *29*, 481.
- (51) Zeng, P.; Zajac, S.; Clapp, P. C.; et al. *Mater. Sci. Eng., A* **1998**, *252*, 301.
- (52) Lehtinen, K. E. J.; Zachariah, M. R. *Phys. Rev.* **2001**, *6320*.
- (53) Friedlander, S. K.; Wu, M. K. *Phys. Rev. B* **1994**, *49*, 3622.
- (54) Gay, J. G.; Berne, B. J. *J. Colloid Interface Sci.* **1986**, *109*, 90.
- (55) Koch, W.; Friedlander, S. K. *J. Colloid Interface Sci.* **1990**, *419*, 140.
- (56) Lehtinen, K. E. J.; Windeler, R. S.; Friedlander, S. K. *J. Colloid Interface Sci.* **1996**, *182*, 606.
- (57) Ehrman, S. H.; Friedlander, S. K.; Zachariah, M. R. *J. Aerosol Sci.* **1998**, *29*, 687.
- (58) Zhu, H. L.; Averbach, R. S. *Mater. Sci. Eng., A* **1995**, *204*, 96.
- (59) Zhu, H. L.; Averbach, R. S. *Mater. Manuf. Processes* **1996**, *11*, 905.
- (60) Zhu, H. L.; Averbach, R. S. *Philos. Mag. Lett.* **1996**, *73*, 27.
- (61) Raut, J. S.; Bhagat, R. B.; Fichthorn, K. A. *Nanostruct. Mater.* **1998**, *10*, 837.
- (62) Heinisch, L. *Synthesis and Processing of Nanocrystalline Powder*; TMS Press: 1996.
- (63) Kim, D. W.; Enomoto, N.; Nakagawa, Z.; et al. *J. Am. Ceram. Soc.* **1996**, *79*, 1095.
- (64) Catlow, C. R. A.; Freeman, C. M.; Royal, R. L. *Physica B* **1985**, *131*, 1.
- (65) Catlow, C. R. A.; James, R. *Proc. R. Soc. London, Ser. A* **1982**, *384*, 157.

- (66) Mostoller, M.; Wang, J. C. *Phys. Rev. B* **1985**, 32, 6773.
(67) Post, J. E.; Burnham, C. W. *Am. Mineral.* **1986**, 71, 142.
(68) Roux, H. L.; Glasser, L. *J. Mater. Chem.* **1997**, 7, 843.
(69) Sawatari, H.; Iguchi, E.; Tilley, R. J. D. *J. Phys. Chem. Solids* **1982**, 43, 1147.
(70) Swamy, V.; Gale, J. D. *Phys. Rev. B* **2000**, 62, 5406.
(71) Oliver, P. M.; Watson, G. W.; Kelsey, E. T.; et al. *J. Mater. Chem.* **1997**, 7, 563.
(72) Collins, D. R.; Smith, W. Council for the Central Laboratory of Research Councils, Daresbury Research Report DL-TR-96-001, 1996.
(73) Bandura, A. V.; Kubicki, J. D. *J. Phys. Chem. B* **2003**, 107, 11072.
(74) Abrahams, S. C.; Bernstein, J. L. *J. Chem. Phys.* **1971**, 55, 3206.
(75) Smith, W. *J. Mol. Graphics* **1987**, 5, 71.
(76) Smith, W.; Forester, T. R. *J. Mol. Graphics* **1996**, 14, 136.
(77) Kumar, K.-N. P.; Keizer, K.; Burggraaf, A. J.; et al. *Nature* **1992**, 358, 48.
(78) Jackson, J. D. *Classical Electrodynamics*; John Wiley & Sons Inc.: 1975.
(79) Ogata, S.; Iyetomi, H.; Tsuruta, K.; et al. *J. Appl. Phys.* **1999**, 86, 3036.